The Role of Atomic Carbon in Directing Electrochemical $CO_{(2)}$ Reduction to Multicarbon Products

Hongjie Peng[1, 3], Michael T. Tang[1, 2, 3], Xinyan Liu[1], Philomena Schlexer Lamoureux[1], Michal Bajdich[1] and Frank Abild-Pedersen[1,*]

[1] SUNCAT Center for Interface Science and Catalysis
SLAC National Accelerator Laboratory
California 94025, USA

[2] Department of Material Science and Engineering
Stanford University California 94305, USA

[3] These authors contributed equally: Hongjie Peng, Michael T. Tang.

* Corresponding Author email: abild@slac.stanford.edu

Abstract

Electrochemical reduction of carbon-dioxide/carbon-monoxide ($CO_{(2)}R$) to fuels and chemicals presents an attractive approach for sustainable chemical synthesis, but also poses a serious challenge in catalysis. Understanding the key aspects that guide $CO_{(2)}R$ towards value-added multicarbon (C_{2+}) products is imperative in designing an efficient catalyst. Herein, we identify the critical steps toward C_2 products on copper through a combination of energetics from density functional theory and micro-kinetic modeling. We elucidate the importance of atomic carbon in directing C_{2+} selectivity and how it introduces surface structural sensitivity on copper catalysts. This insight enables us to propose two simple thermodynamic descriptors that effectively describe C_{2+} selectivity on metal catalysts beyond copper and hence it identifies an intelligible protocol to screen for materials that selectively catalyze $CO_{(2)}$ to C_{2+} products.

The electrochemical reduction of CO_2 and CO paves a promising pathway towards sustainable chemicals and fuels.[1] The mechanism that drives the generation of high-value multicarbon (C_{2+}) products is of particular interest but despite many years of research it still remains elusive.[2, 3] So far elemental copper (Cu) and Cu-based compounds are the only materials that can produce $C_{2(+)}$ hydrocarbons and oxygenates of any significance albeit at high overpotential and with poor selectivity.[4] To optimize Cu-based catalysts or find alternative materials for selective $C_{2(+)}$ production from $CO_{(2)}$, in-depth mechanistic insight is needed in order to untangle the complexities of $CO_{(2)}R$.[5]

Recent experimental efforts have focused on improving the selectivity towards $C_{2(+)}$ products on Cu by tailoring catalyst composition,[6-9] the surface morphology,[10-13] the reaction conditions at the catalyst/electrode interface,[14, 15] and by engineering the electrochemical reactors.[16-18] To identify key intermediates and tie into theoretical efforts, *in situ* or *operando* characterization tools have been employed,[15, 19] but the precise mechanism of the first C–C bond formation is still inconclusive. Inspired by an experimentally observed larger shift with pH in onset potential for C_2 than C_1 products,[20-22] theoretical work has concentrated on coupling steps early in the reduction pathway, specifically CO dimerization.[23-29] The CO dimerization step is strongly affected by solvation and the electric field present at the electrochemical interface,[24, 30] which introduces extra complexity that hinders descriptor-based materials discovery beyond Cu-based catalysts.[31]

In this work, we identify the critical steps of CO reduction (COR) toward C_2 products through density functional theory (DFT) based reaction and activation energies and we introduce an electrochemical microkinetic model that appropriately describes the experimental trends in activity and selectivity. Our model (exemplified on Cu(100)) identifies a potential, U_0, at which the reduction of CO to atomic carbon (C*) via the COH* intermediate exhibits higher rate than either the hydrogen evolution reaction (HER) or the reduction of CO to formyl (CHO*). Subsequently, the surface C* enables thermodynamically favorable coupling with either CO* or gas-phase CO at the interface. In comparison with other pathways including CO dimerization, this process is found to be the dominant C_2 pathway at more reducing potentials, *i.e.*, $U < -0.5$ V vs. the reversible hydrogen electrode (RHE) at pH = 7. This enables a characterization of the C_2 selectivity relative to the single-carbon (C_1) product selectivity through the energetic difference between barriers for dicarbon monoxide (CCO*) and methylidyne (CH*) formation, which further rationalizes the facet dependency of C_2 selectivity on Cu. Finally, this insight allows us to identify two simple descriptors that traces the C_2 selectivity on different metal surfaces at varying potentials: the adsorption energies of CO* and C* (G_{CO*} and G_{C*}).

Reaction pathways for COR. In this paper, we evaluate the CO_2R reaction to C_1 and $C_{2(+)}$ products involving more than two proton-electron transfer (PET) steps. It has been shown and verified both experimentally and theoretically that CO* is the most important common intermediate in COR and CO_2R leading to further reduced products.[4, 20] We therefore focus on CO as the starting reactant in our scheme below. Since Cu is the only catalyst with any significant $C_{2(+)}$ production from $CO_{(2)}$ and since the close-packed (100) surface has been identified as the major exposed facet under reaction conditions[11, 13, 32], we select Cu(100) as our model surface. The role of step sites and defects, which are inherently present to some extent on all surfaces during CO_2R conditions, will be discussed in a later section.

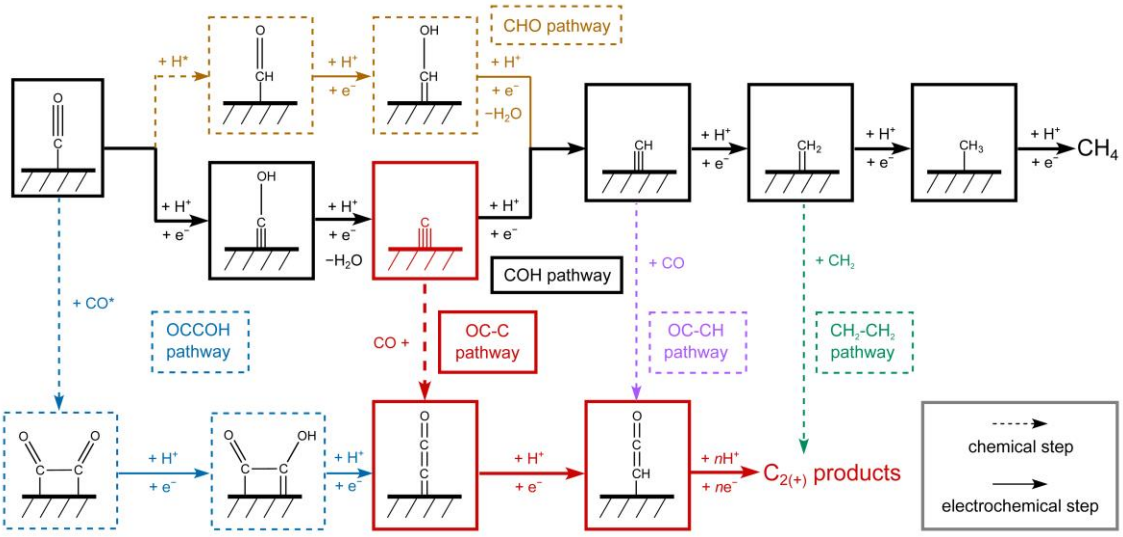

Figure 1. Schematic diagram of reaction steps beyond CO. Pathways toward C_1 (CH_4 as the main product) and C_2 products beyond CO are shown as different colored branches: blue (CHO pathway), black (COH pathway), yellow (OCCOH pathway), red (OC-C pathway), violet (OC-CH pathway), and green (CH_2-CH_2 pathway). Chemical reaction steps are indicated by dashed lines, whereas electrochemical steps are indicated by solid lines. The number of involved PET steps, are increasing from left to right.

In **Figure 1**, the most relevant reactions considered in this work are shown. The production of CH_4 involves CO* initially being reduced to either CHO* or COH*. In a recent study,[33] we showed using simple thermodynamic and kinetic reasoning, that the formation of CHO* is a chemical step preceded by surface hydrogenation whereas COH* is formed through an electrochemical PET step. CH* leading to CH_4 forms as an intermediate in both pathways, either via COH reduction to C* + H_2O or through CHO reduction to hydroxyl methylidyne (CHOH*). A number of intermediates present in the pathway to CH_4 are considered as seeds for $C_{2(+)}$ production; CO* dimerization to OCCO* and subsequent reduction to OCCOH* (OCCOH pathway), CO* coupling with C* to form CCO* (OC-C pathway), CO* coupling with CH* to form CHCO* (OC-CH pathway), and

methylene (CH_2*) dimerization to ethylene (C_2H_4) (CH_2-CH_2 pathway). In accordance with previous studies, we only consider OCCOH* as the protonation product of OCCO* and exclude coupling of CO with CHO*, CHOH*, and COH* due to higher barriers than their protonation counterparts.[23, 27, 28, 34] The above considered C_2 pathways except for the CH_2 dimerization lead to the formation of CHCO* and based on previous thermodynamic analyses,[23, 28] all subsequent reaction steps toward $C_{2(+)}$ products are assumed to be downhill in energy.

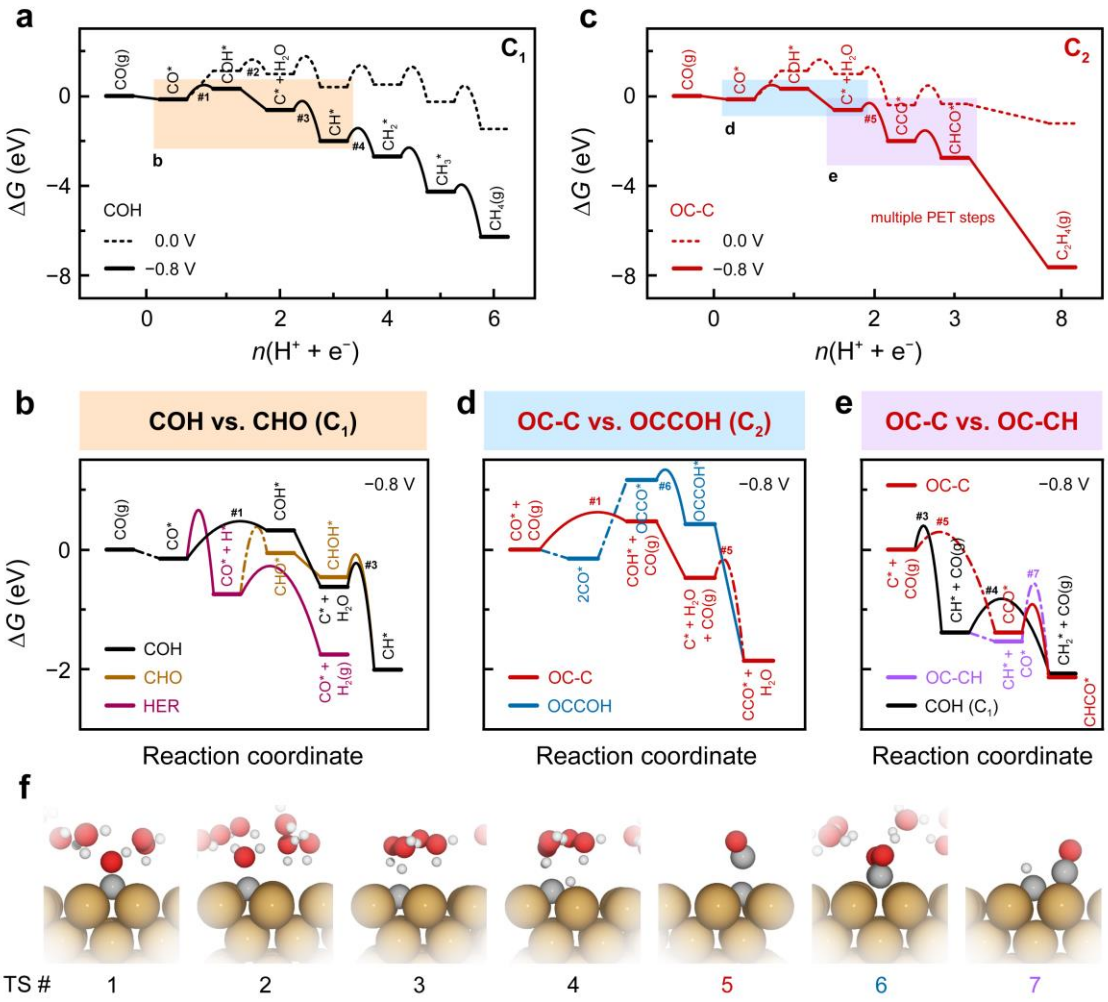

Figure 2. Free energy diagrams (FEDs) of COR on Cu(100). (**a**) FEDs at potentials $U = 0.0$ V and $U = -0.8$ V, showing the COH pathway - the dominant C_1 pathway toward CH_4. The yellow square highlights the major steps competing with the CHO pathway and the HER shown in (**b**). (**b**) FEDs at potential $U = -0.8$ V, showing the competition between C_1 pathways: COH (black), CHO (brown), and the HER (wine). (**c**) FEDs at $U = 0.0$ V and $U = -0.8$ V, showing the OC-C pathway - the dominant C_2 pathway. C_2H_4 is used as the representative $C_{2(+)}$ product. The blue and violet squares highlight the major steps competing with the OCCOH pathway and the OC-CH pathway, shown in (**d**) and (**e**), respectively. (**d**) FEDs at potential $U = -0.8$ V, showing the competition between C_2 pathways OC-C (red), OCCOH (blue). (**e**) FEDs at potential $U = -0.8$ V, showing the competition between C_2 pathways OC-CH (violet), and the COH pathway toward C_1 (black). All the potentials are referenced to the RHE scale at pH = 7. Note that there are chemical steps competing with electrochemical steps at the same

number (*n*) of PETs and hence the scale of the *x*-axes in (**a**) and (**c**) are non-uniform. These chemical steps are shown as the dash-dotted lines in (**b**, **d**, and **e**). (**f**) Shows transition state structures of key elementary steps with the indexes indicated in (**a**–**e**): 1. CO-H protonation to COH*, (2) COH-H protonation to C* + H_2O, (3) C-H protonation to CH*, (4) CH-H protonation to CH_2*, (5) C-CO coupling with CO from the gas phase, (6) OCCO-H protonation to OCCOH*, and (7) OC-CH surface coupling.

Figures 2a–e depicts the Gibbs free energetics of competing pathways, as proposed in **Figure 1**, at applied potentials of 0.0 V and −0.8 V vs. the reversible hydrogen electrode (RHE) on Cu(100). Throughout we apply the RHE scale unless stated otherwise. The potential of −0.8 V was chosen as it is the value at which substantial multicarbon products begin forming on Cu in $CO_{(2)}R$ under neutral pH conditions.[20, 21, 35] For all chemical steps the adsorption energies and barriers were calculated in vacuum and all electrochemical barriers were obtained using an explicit solvent model combined with the charge-extrapolation method.[36] The relevant transition state (TS) structures are shown in **Figure 2f**.

At low overpotentials, the COH-H protonation is identified as the rate-determining step (RDS) of the COH pathway (**Figure 2a**). With increasing overpotential, the RDS of the COH pathway shifts to the CO-H protonation step, which possesses lower barriers than both the HER and the CHO pathway (**Figure 2b**). Within a wide potential window, the COH pathway is more favorable than HER and the CHO pathway (even if the CHO path is considered an electrochemical step) (**Supplementary Fig. 1**). Consequently, C* becomes available on the surface under these conditions, thus opening up pathways of either further protonation (**Figure 2a**) or coupling with CO **(Figure 2b**), leading to C_1 or C_2 products, respectively. We have considered coupling C* with CO on the surface or in the gas phase and find that on Cu(100), C* coupling to gas-phase CO possesses a lower barrier, 0.31 eV, compared with surface coupling, 0.73 eV (**Supplementary Fig. 2**). Such a low barrier agrees well with facile low-temperature CO dissociation on Cu induced by C-CO coupling.[37] Because the coupling barrier is independent of the applied potential and CO couples strongly to surface C* on Cu(100), the CCO formation from C* is more favorable at low overpotentials ($U > -0.88$ V) than the potential dependent CH formation, thus resolving the experimentally observed earlier onset potential for C_2 than for C_1.[20, 21, 35]

To further validate that the C* bifurcates exclusively into either C_1 or C_2 products, a number of possible competing pathways, all shown in **Figure 1** are considered in our analysis. The conventional CO dimerization pathway is found to possess a high reaction energy from two adsorbed CO* to OCCO* (1.31 eV), thereby being less dominant when compared to the OC-C pathway at sufficiently negative potentials (*e.g.* −0.8 V) (**Figure 2d**). We note that the energetics of CO dimerization, are significantly affected by the electrochemical environments (*i.e.*, solvent, ion, and pH) and we will discuss these effects on the reaction pathways in a later section. The

coupling between CO* and CH* is limited by two factors: (1) the C* protonation to produce sufficient CH* requires high overpotentials ($U < -0.88$ V) to compete with the CCO formation and (2) at high overpotentials, however, the CH-H protonation barrier becomes lower than the potential independent OC-CH coupling barrier (**Figure 2e**). Similar arguments apply for CH_2 dimerization: insufficient CH_2* at low overpotentials, whereas the dimerization cannot compete with the electrochemical CH_2-H protonation at higher overpotentials ($U < -0.21$ V) (**Supplementary Fig. 3**).

Microkinetic model of COR. To further illustrate the role of C*, a mean-field microkinetic model is developed considering adsorbate-adsorbate interactions in a self-consistent way.[34] Given the intrinsic DFT errors (±0.15 eV), the uncertainties brought by the parameterization of the adsorbate-adsorbate interactions, and the variations in the solvent structure affecting the electrochemical barriers, the microkinetic model can only serve as a tool for qualitative comparison with experimental trends in activity and selectivity.

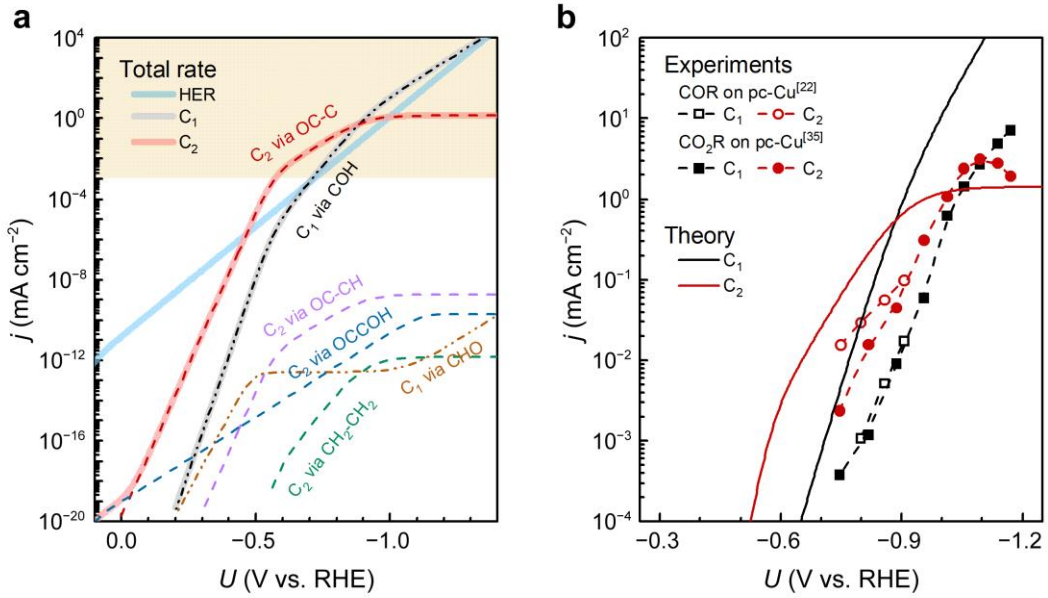

Figure 3. Theoretical and experimental polarization curves of $CO_{(2)}R$ on Cu(100) (pH = 7). (**a**) Theoretical polarization curves showing the total rates of HER, C_1, and C_2, as well as the partial contribution of each pathway to the current density (j). The dash-dotted lines show the partial contribution by C_1 pathways and the dashed lines correspond to the C_2 pathways. (**b**) The comparison between theoretical COR and experimental $CO_{(2)}R$ polarization curves. The experimental curves of COR and CO_2R are obtained on pc-Cu from Ref. [22] and Ref. [35], respectively.

Figure 3a shows the theoretical polarization curves for the total current of HER, C_1, and C_2, as well as the partial current of each pathway across potentials vs. RHE. Clearly the theoretical

total currents follow the same trend as the energetics revealed in **Figure 2** and **Supplementary Fig. 1**: When $U > -0.45$ V, the barrier for the Volmer step is smaller than the energy difference between CO* and the TS of COH-H protonation and thus HER is the dominant pathway; when -1.40 V $< U < -0.45$ V, the RDS shifts to the first protonation step (CO* to COH) and thus it controls the overall rate of C_1 and C_2 relative to HER; and when $U < -1.40$ V, the Volmer barrier, having a larger charge transfer coefficient, β,[38] decreases faster than the CO-H protonation and thus HER dominates again below this potential.

In the potential window, -1.40 V $< U < -0.45$ V, where COR is dominant, C_1 rates are found to exceed C_2 rates at $U = -0.88$ V where the C-CO coupling barrier becomes higher than the electrochemical C-H protonation barrier. The fluctuations in the relative energetic barriers between competing pathways results in product distributions from microkinetic modeling that align with the trends seen in experiments (**Supplementary Fig. 4**).[21] The partial contributions from each pathway as shown in **Figure 3a** reflect the free energetics in **Figures 2a–e**, showing the electrochemical COH pathway and the OC-C pathway as the two dominant pathways that lead to C_1 and C_2 products, respectively. Further comparison with the experimental polarization curves of COR and CO_2R on polycrystalline Cu (pc-Cu) electrodes underscores the capability of our model in accurately predicting the potential-dependent variations in activity and selectivity (**Figure 3b**).

Solvation, field, and pH effects. To include the effects of solvation and field stabilization, we studied the energetics of key intermediates by applying an explicit solvent model (**Supplementary Note 1**) and introducing a field at the interface of -0.6 V Å^{-1} (**Supplementary Fig. 5**). In the presence of solvents and ions, the interfacial hydrogen bonds and electric fields stabilize the OCCO* significantly compared to the energetics presented in **Figure 2**. The solvation/field stabilization to key intermediates (OCCO* and OCCOH*) in the OCCOH pathway is found to be considerably more profound than that to intermediates (COH* and C*) in the OC-C pathway (**Supplementary Fig. 6**). Nevertheless, we find that as long as a certain negative potential is reached to drive the reduction of CO to C*, the formation of CCO* from C* is always more favorable than CO dimerization (**Figure 4a**). Regardless of solvation or local field effects, C* becomes the key intermediate that directs C_1 and C_2 selectivity on Cu below that potential. Applying these energetic corrections from solvation and electric field induces minor changes to the prediction of the dominant pathway at pH = 7 (**Figure 4b** and **Supplementary Fig. 8a**). On Cu(100) under adequate reducing potentials, the solvation/field-intensified OCCOH pathway cannot compete against the OC-C pathway. Considering the stronger solvation/field stabilization to CCO* and the corresponding TS of C-CO than C* and CH* (**Supplementary Fig. 7**), our model is still able to

rationalize the experimentally observed change in C_{2+} selectivity that a local field induces.[9, 14]

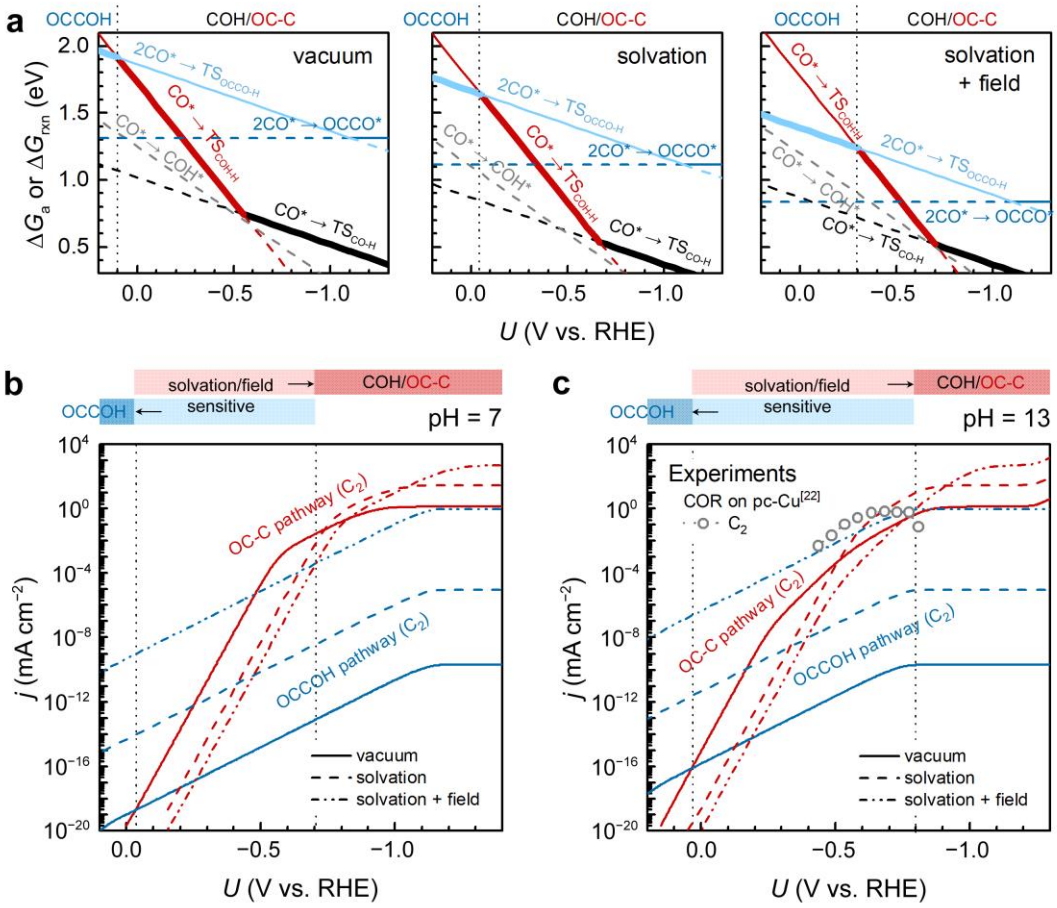

Figure 4. Reaction energetics and microkinetic modeling, including solvation, field, and pH effects. (**a**) Potential dependent reaction energies (ΔG_{rxn}) and activation energies (ΔG_a) for the RDSs in the COH/OC-C pathway (black/red) and the OCCOH pathway (blue) at pH = 7. Energies obtained at various simulation conditions are plotted: vacuum (left), with solvation correction (middle), and with solvation correction and electric field stabilization (field strength: −0.6 V Å^{-1}) (right). (**b, c**) Theoretical polarization curves showing the partial contribution to the C_2 current density of the COH/OC-C pathway (red) and the OCCOH pathway (blue) at (**b**) pH = 7 and (**c**) pH = 13. The potential window where the solvation/field effect changes the dominant pathway is marked. The comparison between theoretical and experimental COR polarization curves at pH = 13 are also shown in (**c**). Experimental curves of COR are obtained on pc-Cu from Ref. [22].

We also consider COR under alkaline conditions, where experiments generally are performed at roughly pH = 13.[21, 22] At these conditions, our model predicts the OCCOH pathway as plausible (**Figure 4c**). Experimental COR toward C_2 products at pH = 13 encounters transport limitations at $U < -0.8$ V, thereby inhibiting a direct comparison to theoretical predictions of OC-C coupling (**Supplementary Fig. 8b**).[22] Furthermore, the OC-C pathway is overtaken by the COH (C_1) pathway due to the potential dependency of the C-H protonation barrier at a standard hydrogen electrode (SHE) scale as opposed to the C-CO coupling barrier.[34] Noteworthy, several issues of

alkaline $CO_{(2)}R$ limits the conversion efficiency, such as carbonate formation for CO_2R[16] and low single-pass conversion efficiency for COR.[17, 18, 39] For these reasons, our main focus is on mechanistic aspects and materials discovery for $CO_{(2)}R$ at neutral pH, where the OC-C pathway is shown to be relevant.

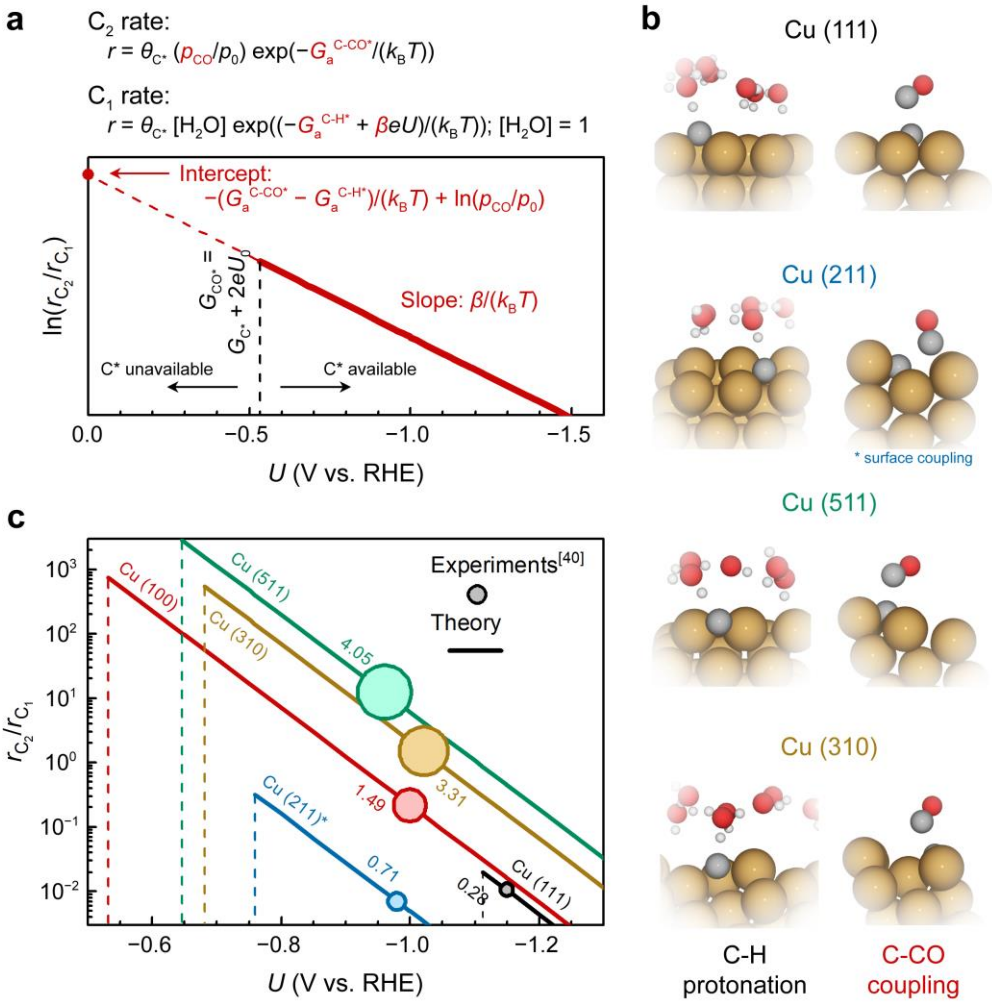

Figure 5. Facet dependent selectivity of C_2 on Cu (pH = 7). (**a**) Schematic illustration of the potential-dependent C_2 selectivity over a certain facet, showing the expression for onset potential U_0, slope, and intercept. The critical parameters that direct the C_2 selectivity include the activation barriers of CCO and CH formation, the partial pressure of CO, and the charge coefficient of C-H protonation. (**b**) Transition state structures of C-H protonation and C-CO coupling on various Cu facets. (**c**) Potential-dependent C_2 selectivity on Cu(111), Cu(211), Cu(511), Cu(100), and Cu(310). The theoretically predicted r_{C_2}/r_{C_1} are plotted as solid lines whereas corresponding vertical dash lines indicate the onset potential U_0 for CO protonation and hence the formation of C* on the surface. The experimental numbers for r_{C_2}/r_{C_1} are obtained from Ref. [40] and are shown as circles of different size. The center of each circle is located on the corresponding theoretical line at the applied potential indicated in Ref. [40]. The size of each circle is proportional to the exact experimental r_{C_2}/r_{C_1} value, which is shown. The theoretical trend in the facet dependencies agrees well with the experiments. (* On Cu(211), CO couples with C* via a surface mediated mechanism due to a geometric constraint, thus, the intercept in (**a**) is expressed as $\ln(\theta_{CO*}) + \frac{-G_a^{OC\text{-}C} + G_a^{C\text{-}H}}{k_B T}$ for Cu(211)).

Facet dependent selectivity of C_2 on Cu. Our approach and microkinetic modeling enables us to identify four key reaction steps that determines the $CO_{(2)}R$ activity and selectivity:

(i) $CO^* \text{ (or } CO(g) + *) + H^+ + e^- \rightarrow COH^*$ (CO-H protonation)

(ii) $CO^* \text{ (or } CO(g) + *) + 2(H^+ + e^-) \rightarrow C^* + H_2O$ (C formation)

(iii) $CO(g) \text{ (or } CO^*) + C^* \rightarrow CCO^*$ (C-CO coupling)

(iv) $C^* + H^+ + e^- \rightarrow CH^*$ (C-H protonation)

Here reaction (i) and (ii) determine the overall rate which explicitly accounts for the shift in RDS with applied potential. The competition between reaction (iii) and (iv) determine the selectivity.

Based on our microkinetic model and a simple quasi-equilibrium assumption, surface C* will become accessible at a certain potential, U_0, defined by the condition; $\Delta G^{(ii)}_{rxn} = 0$. Drawing on the computational hydrogen electrode model, $\Delta G^{(ii)}_{rxn}$ can be written as $G_{C^*} - G_{CO^*} \text{ (or } G_{CO(g)}) + 2eU$) and thus $U_0 = (G_{C^*} - G_{CO^*} \text{ (or } G_{CO(g)}))/(-2e)$. When $U < U_0$, the forward rates of reaction (iii) and reaction (iv) are given by:

$$r_{C_2} = A\theta_{C^*}\theta_{CO^*} \exp\left(-\frac{G_a^{OC\text{-}C}}{k_B T}\right) + A\theta_{C^*}\left(\frac{p_{CO}}{p_0}\right) \exp\left(-\frac{G_a^{C\text{-}CO}}{k_B T}\right)$$

$$r_{C_1} = A\theta_{C^*}[H_2O] \exp\left(-\frac{G_a^{C\text{-}H} + e\beta U_{RHE}}{k_B T}\right)$$

where A is a pre-exponential factor, k_B Boltzmann's constant, T the absolute temperature, θ_{C^*} and θ_{CO^*} are surface coverages of C* and CO*, respectively, (p_{CO}/p_0) is the partial pressure of gas-phase CO, and $G_a^{OC\text{-}C}$, $G_a^{C\text{-}CO}$, and $G_a^{C\text{-}H}$ are forward activation energies of C-CO surface coupling, C-CO gas-phase coupling, and C-H protonation at $U = 0$ V vs. RHE, respectively. The charge transfer coefficient for the C-H protonation step, β, is set to be 0.5. Since both $\Delta G^{(iii)}_{rxn}$ and $\Delta G^{(iv)}_{rxn}$ are considerably downhill in energy when $U < U_0$, only the forward rates are considered. According to a previous analysis,[41] we only regard molecular water as the proton donor within the relevant pH range (pH > 4), at which $[H_2O] = 1$ is a reasonable assumption. In this study, all facets Cu(100), Cu(111), Cu(511), Cu(310), except for Cu(211) exhibit much larger $G_a^{OC\text{-}C}$ than $G_a^{C\text{-}CO}$ (**Table 1**), hence the expression for the C_2 rate is given by:

$$r_{C_2} = A\theta_{C^*}\left(\frac{p_{CO}}{p_0}\right) \exp\left(-\frac{G_a^{C\text{-}CO}}{k_B T}\right)$$

If we assume similar pre-exponential factors, the selectivity of C_2 over C_1 can be expressed as:

$$\ln\left(\frac{r_{C_2}}{r_{C_1}}\right) = \ln\left(\frac{p_{CO}}{p_0}\right) + \frac{-G_a^{C\text{-}CO} + G_a^{C\text{-}H} - e\beta U_{RHE}}{k_B T}$$

This result enables a quantitative assessment of the slope and intercept of $\ln(r_{C_2}/r_{C_1})$ as well as the

mapping of selectivity as a function of potential as shown in **Figure 5a**.

Table 1. A summary of the $G_a^{OC\text{-}C}$, $G_a^{C\text{-}CO}$, and $G_a^{C\text{-}H}$ on various Cu facets.

Cu facets	$G_a^{OC\text{-}C}$ (eV)	$G_a^{C\text{-}CO}$ (eV)	$G_a^{C\text{-}H}$ (eV)
(100)	0.73	0.31	0.80
(111)	---	0.15	0.63
(211)	0.46	---	0.80
(511)	0.49	0.27	0.84
(310)	0.69	0.30	0.85

Note: the OC-C barrier calculation on Cu(111) and C-CO barrier calculation on Cu(211) automatically relax to the C-CO and OC-C mechanism, respectively. Hence, the corresponding barriers are unavailable.

Since the transition state structures of C-H protonation and C-CO coupling shown in **Figure 5b** are very similar on different Cu facets, the above expression possesses certain generality when analyzing C_2 over C_1 selectivity. **Figure 5c** depicts the theoretical trends in C_2 selectivity on different Cu single-crystal electrodes. Cu(511), Cu(310), and Cu(100) are very selective towards C_2 at low overpotentials (−0.7 to −0.9 V). Cu(211) is seen to have a higher barrier, $G_a^{OC\text{-}C}$, compared to the other facets and therefore it is less selective, whereas Cu(111) possesses a low $G_a^{C\text{-}CO}$ which automatically result in a favored C_2 selectivity. However, the limiting factor on Cu(111) is the instability of C*, which results in a very low U_0 and thus an inferior C_2-selectivity for this surface. Overall, the observed facet dependency is rationalized by the greater stabilization of atomic C* on Cu (100)-like sites. This characteristic four-fold geometry, combined with the unique energetics associated with Cu is what causes the favored selectivity of C_2 over C_1 products. These trends are in good agreement with experimentally observed facet dependencies by Hori et al.,[40] demonstrating the remarkable ability of our model to describe the structure sensitivity of $CO_{(2)}R$ catalysts. The facet dependency insight achieved through the simple expression of $\ln(r_{C_2}/r_{C_1})$ above, also enables us to rationalize how to enhance the C_{2+} selectivity by tuning the effective CO pressure/concentration. Strategies such as system pressurization,[22] tuning the $CO_{(2)}$ gradient,[14] CO/CO_2 co-feeding,[42] and doing the electrocatalysis in tandem[8, 42] have been experimentally explored.

Selectivity maps with G_{CO*} and G_{C*} as descriptors. With the above study on different Cu facets, we note that the energetic analysis through reactions (i)–(iv) is sufficient to qualitatively unveil the trends in $CO_{(2)}R$ activity and selectivity. Considering that their reaction energies can be adequately described through scaling by G_{CO*} and G_{C*} (**Supplementary Fig. 9**), we can therefore create a map across various metals that expresses their selectivity towards C_1 and C_2 products. To show the importance of four-fold

sites in stabilizing the C* intermediate, we include the (100), (111), (211) facets on other metals. The results clearly indicate the necessity of including the binding energy of C* in such sites as a material screening descriptor towards improved C_2 product selectivity. Note that similar maps using binding strengths of CO and OH as descriptors for selectivity towards C_1 products have been introduced by authors recently.[33]

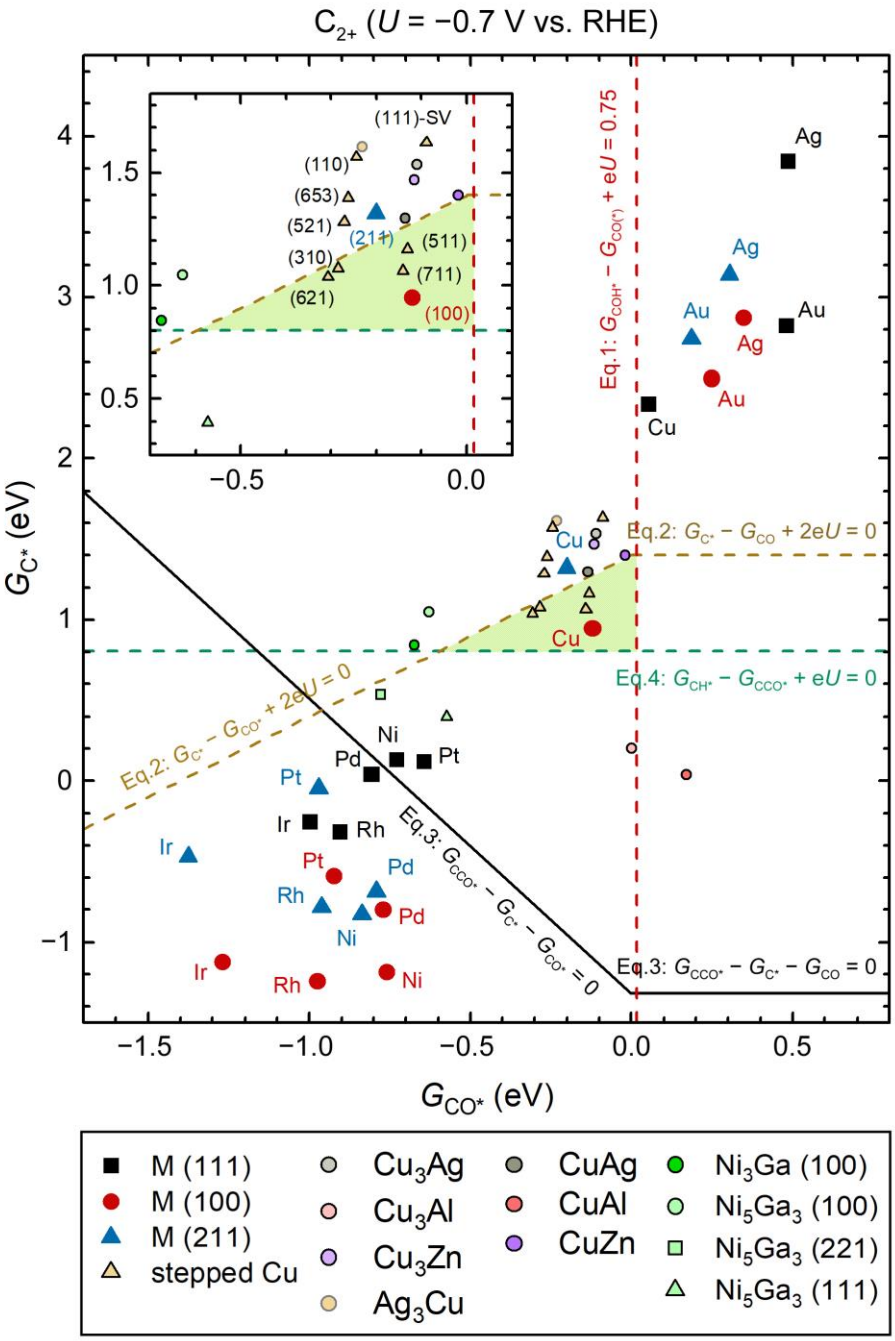

Figure 6. Descriptor-based (G_{CO*}, G_{C*}) selectivity map at U = −0.7 V (vs. RHE at pH = 7). The C_2-selective region is highlighted in light green. Various metallic and intermetallic systems are included with

symbols as indicated in the legend. The detailed surface orientations and computational details can be found in the Supplementary Material. Square, circular,and triangular symbols correspond to surfaces with three-fold terrace sites, four-fold terrace sites, and under-coordinated step sites, respectively. Electrochemically driven processes are shown as dashed lines and the potential-independent C-CO coupling process is indicated with solid lines.

As shown in **Figure 6**, our map uses simple thermodynamic conditions based on the reaction energies (ΔG_{rxn}) for reactions (i)–(iv):

CO to COH* acceptable rate (TOF 1 s^{-1} $site^{-1}$ at 300K):	$\Delta G^{(i)}_{rxn} < 0.75$ eV	(Eq. 1)
CO reduction to kinetically accessible C*:	$\Delta G^{(ii)}_{rxn} = 0$	(Eq. 2)
C-CO coupling more favorable than CO adsorption:	$\Delta G^{(iii)}_{rxn} < G_{CO*}$	(Eq. 3)
C-CO coupling more favorable than C-H protonation:	$\Delta G^{(iv)}_{rxn} < \Delta G^{(iii)}_{rxn}$	(Eq. 4)

Under further lowering of the potential, CO-H protonation eventually becomes the RDS of $CO_{(2)}R$ toward C_1/C_2 products with a forward barrier close to the reaction free energy $\Delta G^{(i)}_{rxn}$ (**Figure 4a**). We therefore use $\Delta G^{(i)}_{rxn}$ as an estimate of the barrier for the RDS in our thermodynamic analysis and assign a turnover frequency of ~1 s^{-1} per site at 300K as the lowest acceptable overall $CO_{(2)}R$ rate. Such a rate corresponds to the condition defined by Eq. 1. To accurately describe the effect of CO adsorption, we replace G_{CO*} in Eqs. (1–3) with $G_{CO} = 0$ when the adsorption of CO on the catalytic surface is unfavorable ($G_{CO*} > 0$).

Clearly, the C_2 selectivity changes with applied potential and at −0.7 V vs. RHE, the above thermodynamic conditions form a triangular region (marked in light green in **Figure 6**) where a decent overall $CO_{(2)}R$ rate can be obtained and where CCO* is thermodynamically favored over CH* formation. This map presents a powerful tool, as it is capable of qualitatively discerning C_1 and C_2 product selectivity across all metals at different applied potentials. Remarkably, all known C_2 selective Cu facets: Cu(100), Cu(310), Cu(511) and Cu(711) fall near the center of the region at this potential. It is noteworthy, that,Cu(211) sits on the edge of the region, whereas Cu(111) is unable to catalyze $CO_{(2)}R$ to C_2 or C_1 at such low overpotential. Our theoretical trends are based entirely on simple thermodynamic arguments, though they are in agreement with the sophisticated kinetics analysis used in the previous section. In short, the thermodynamic selective map is sufficient to qualitatively describe the $CO_{(2)}R$ selectivity across a large span of materials space.

Furthermore, the map in **Figure 6** also shows the narrow potential window of opportunity to form C_2 products. The ability to form surface carbon, C* defined by Eq. 2 and thus C_2 products will shift towards more noble materials at more negative potentials. However, the thermodynamic driving force for CH* formation (Eq. 4) shifts in the same direction, however, much faster. This leads to a narrowing of the window for potential catalysts with selective C_2 production and to a widening of the window for

selective CH_4 producing catalysts (**Supplementary Fig. 10–11**). This effect accentuates the challenge in identifying C_2-selective catalysts beyond Cu, Cu-based alloys, and intermetallics. It also highlights the role of (100)-like facets in the selectivity towards C_2 products over C_1 products since the above narrow window for C_2 production does not include materials with dominant (111)-like facets (**Supplementary Fig. 12–13**).

Regarding metals different from Cu, our potential dependent selectivity maps (**Figure 6** and **Supplementary Fig. 10–11**) show very few candidates that fall in the C_2-selective region. Ag and Au do not form C_2 because of their poor C* binding energies, strong-binding metals can easily reduce CO to C* but the C* on these surfaces is not as reactive as on more noble metals like Cu to enable the C-CO coupling step rather than CO adsorption. More promising systems relevant from experimental results, such as Cu-based alloys,[6, 7] Ni-Ga intermetallics,[43] as well as defective Cu (modeled as Cu(111) with a single vacancy, denoted as (111)-SV),[11, 13] are also plotted on the map as shown on **Figure 6**. These materials all lie in the vicinity of the C_2 selective region, which rationalizes recent experimental observations including enhanced C_2 production on Cu-Zn (Cu_3Zn in the map),[6] Cu-Ag (Cu_3Ag in the map),[7] and defective Cu nanoparticles,[11, 13] and traced C_2 activity on Ni-Ga systems.[43]

Verification of OC-C pathway toward C_2. While the OC-CO pathway has been successful in describing the pH independent behavior of C_2 rates on Cu surfaces, we note in the following several observations that cannot easily be understood from a pathway involving CO dimerization, which on the other hand can be explained by the COH and OC-C pathway.

Experimentally surface-carbon-induced deactivation of Cu and Ag catalysts during $CO_{(2)}R$[44, 45] can only be attained through coupling of atomic carbon rather than decomposition of CH_x species. Because of the inability of both Cu and Ag to break the C–H bond at room temperature,[46] atomic carbon must be present as an intermediate during $CO_{(2)}R$, thus supporting the COH pathway. Once C* is available, we have demonstrated the predominance of C-CO coupling under an applied potential $U < U_0$ at pH = 7 (**Figure 2** and **Figure 4**).

CO dimerization on Au exhibits a ΔG_{rxn} of only 0.50 eV (~0.37 eV lower than Cu) considering the same solvation and electric field conditions as on Cu. These conditions should therefore restrain desorption of CO from Au surfaces and hence, Au should in principle be a particularly selective catalyst toward C_2 products through the CO dimerization. This, however, has never been experimentally validated.

Despite reasonable solvation/field stabilization, Ni-rich Ni_3Ga(100) and (111) surfaces were found unable to stabilize OCCO*, whereas on Pt(100) with a comparable CO binding strength to Ni, the ΔG_{rxn} for CO dimerization was calculated to be 1.86 eV, almost insurmountable at room

temperature. Hence, we do not expect CO dimerization to account for the observed C_2 production on Ni-Ga intermetallics.[43] The observed earlier onset potential for C_2 products on Ni-Ga intermetallics than Cu, however, can be well understood based on the OC-C mechanism as shown in **Supplementary Fig. 10**.

The OC-C mechanism offers the ability to rationalize the above experimental observations with regards to material screening, whereas the CO dimerization mechanism inadequately does. This suggests that understanding the role of atomic carbon in the $CO_{(2)}R$ provides the necessary insight into the reaction mechanism and paves the way for discovery of new materials. Future work will focus on descriptor-based high-throughput screening of potential $CO_{(2)}R$ catalysts based on this model and further refinement of the model to enable the construction of a kinetic volcano, to interface the kinetics with transport models, and to exploit reaction pathways toward C_3/C_4 products.

In conclusion, we have identified the relevant reaction pathways for CO and CO_2 reduction towards further reduced C_1 (methane) and C_{2+} based on first principles reaction energetics and micro-kinetic modeling. We elucidated the importance of atomic carbon as the key surface intermediate that directs the C_1/C_{2+} selectivity through two distinct competing reaction pathways. Our model enables quantification of experimentally observed activity/selectivity trends for $CO_{(2)}R$ on Cu at varying potentials and changes in surface orientation. We also demonstrated that with the two simple thermodynamic descriptors, CO and C binding strengths, a number of experimental observations can be rationalized across a range of metal and metal alloy catalysts. In particular, four-fold terrace sites on Cu-like materials were identified as strongly C_{2+}-selective, however only within a narrow potential window. These insights enable us to identify the immense challenges associated with the search for new materials that are similar or even surpass Cu in terms of activity and selectivity.

Calculation Details

Reaction energetics were calculated with DFT with a periodic plane-wave implementation and ultrasoft pseudopotentials using the QUANTUM ESPRESSO code,[47] interfaced with the Atomistic Simulation Environment (ASE).[48] We applied the BEEF-vdW functional, which provides a reasonable description of van der Waals forces while maintaining an accurate prediction of chemisorption energies.[49] Plane-wave and density cutoffs were 500 and 5000 eV, respectively, with a Fermi-level smearing width of 0.1 eV. The adsorption energies on (111) and (100) surfaces of *fcc* transition metals were evaluated using four-layer (3 × 3) supercells with the bottom two layers constrained and a vacuum layer of 20 Å, and [4 × 4 × 1] Monkhorst-Pack *k*-point grids[50] were used. The simulation of (211) surfaces of *fcc* transiton metals followed the same calculation settings but on four-layer (1 × 3) supercells. (3 × 1) supercells were also used to model Cu(310) and Cu(511) and Monkhorst-Pack *k*-point grids are [3 × 6 × 1] and [4 × 4 × 1], respectively. All the cell sizes and corresponding Monkhorst-Pack *k*-point grids for other Cu facets and intermetallic surfaces could be found in **Supplementary Table 5**. The solvation and field corrections considered in this work are shown in **Supplementary Note 1**. Modified psLib ultrasoft pseudopotentials were chosen. All structures were optimized until the force components were less than 0.05 eV $Å^{-1}$. A dipole correction was applied to decouple the electrostatic interaction between the periodically repeated slabs.

Electrochemical barriers were calculated with (3 × 3) and (4 × 3) supercells and Monkhorst-Pack k-point grids of [4 × 4 × 1] and [3 × 4 × 1], respectively. All structures contained a three-layer transition metal slab, with atoms in the top layer relaxed and the rest fixed, along with a hydrogen-bonded water layer determined through minima hopping.[24] We considered the barriers from several different water structures, the lowest of which should dominate the activity. Transition state geometries and energies were calculated using the climbing-image nudged elastic band (CI-NEB) method, with the forces on the climbing image converged to less than 0.05 eV $Å^{-1}$.[51] The spring constants were tightened for images close to the saddle point.[52] The plane wave and charge density cutoff, exchange-correlation functional, and other parameters were the same as those used for geometry optimizations. The charge extrapolation method[36, 38] was used to deduce the activation barriers at constant potential.[53] All transition states were referenced to the initial state of aqueous protons and electrons in bulk solution, as determined using the computational hydrogen electrode.[54]

We have applied an overbinding correction to CO adsorption energies on strong-binding metals (Ir, Rh, Pt, Pd, and Ni) due to generalized gradient approximations (GGA) functionals generally positioning the unfilled 2π* orbital at too low energy. The correction is based on the vibrational frequency of the internal CO stretch mode of *CO, relative to the frequency in

vacuum.[55] The vibrational frequencies can be found in **Supplementary Table 6**. Mean-field microkinetic models are simulated with the CATMAP software package.[56] The details could be found in **Supplementary Note 2**. All relaxed structures and energetics are available on the Catalysis-Hub database.[57]

Acknowledgements

This material is based upon work performed by the Joint Center for Artificial Photosynthesis, a DOE Energy Innovation Hub, supported through the Office of Science of the U.S. Department of Energy under Award Number DE-SC0004993. We acknowledge the use of the computer time allocation for the Material Simulations in Joint Center for Artificial Photosynthesis (JCAP) at the National Energy Research Scientific Computing Center, a DOE Office of Science User Facility supported by the Office of Science of the U.S. Department of Energy under Contract No. DE-AC02-05CH11231. P.S.L. gratefully acknowledges the Alexander von Humboldt Foundation (AvH) for financial support. The authors thank Dr. Tao Wang and Dr. Alan C. Luntz for insightful discussions and helpful suggestions.

Author contributions

F.A.P. conceived the project. H.P. and M.T.T. contributed all calculations of adsorption energies. H. P., M.T.T., and X.L. contributed all calculations of activation barriers. H.P. and X.L. contributed microkinetic modeling. H.P., M.T.T., and F.A.P. contributed analysis of data and writing. All authors contributed towards writing and discussion.

References

1. De Luna, P. et al. What would it take for renewably powered electrosynthesis to displace petrochemical processes? *Science* **364**, eaav3506 (2019).
2. Gao, D. F., Aran-Ais, R. M., Jeon, H. S. & Cuenya, B. R. Rational catalyst and electrolyte design for CO_2 electroreduction towards multicarbon products. *Nat. Catal.* **2**, 198-210 (2019).
3. Ross, M. B. et al. Designing materials for electrochemical carbon dioxide recycling. *Nat. Catal.* **2**, 648-658 (2019).
4. Nitopi, S. et al. Progress and perspectives of electrochemical CO_2 reduction on copper in aqueous electrolyte. *Chem. Rev.* **119**, 7610-7672 (2019).
5. Birdja, Y. Y. et al. Advances and challenges in understanding the electrocatalytic conversion of carbon dioxide to fuels. *Nat. Energy* **4**, 732-745 (2019).
6. Ren, D., Ang, B. S. H. & Yeo, B. S. Tuning the selectivity of carbon dioxide electroreduction toward ethanol on oxide-derived Cu_xZn catalysts. *ACS Catal.* **6**, 8239-8247 (2016).
7. Clark, E. L., Hahn, C., Jaramillo, T. F. & Bell, A. T. Electrochemical CO_2 reduction over compressively strained CuAg surface alloys with enhanced multi-carbon oxygenate selectivity. *J. Am. Chem. Soc.* **139**, 15848-15857 (2017).
8. Morales-Guio, C. G. et al. Improved CO_2 reduction activity towards C_{2+} alcohols on a tandem gold on copper electrocatalyst. *Nat. Catal.* **1**, 764-771 (2018).
9. Li, F. et al. Molecular tuning of CO_2-to-ethylene conversion. *Nature* doi: 10.1038/s41586-019-1782-2 (2019).
10. Roberts, F. S., Kuhl, K. P. & Nilsson, A. High selectivity for ethylene from carbon dioxide reduction over copper nanocube electrocatalysts. *Angew. Chem. Int. Ed.* **54**, 5179-5182 (2015).
11. Kim, D., Kley, C. S., Li, Y. F. & Yang, P. D. Copper nanoparticle ensembles for selective electroreduction of CO_2 to C_2-C_3 products. *Proc. Natl. Acad. Sci. U. S. A.* **114**, 10560-10565 (2017).
12. Jiang, K. et al. Metal ion cycling of Cu foil for selective C-C coupling in electrochemical CO_2 reduction. *Nat. Catal.* **1**, 111-119 (2018).
13. Huang, J. F. et al. Potential-induced nanoclustering of metallic catalysts during electrochemical CO_2 reduction. *Nat. Commun.* **9**, 3117 (2018).
14. Singh, M. R., Kwon, Y., Lum, Y., Ager, J. W. & Bell, A. T. Hydrolysis of electrolyte cations enhances the electrochemical reduction of CO_2 over Ag and Cu. *J. Am. Chem. Soc.* **138**, 13006-13012 (2016).
15. Yang, K. L., Kas, R. & Smith, W. A. In situ infrared spectroscopy reveals persistent alkalinity near electrode surfaces during CO_2 electroreduction. *J. Am. Chem. Soc.* **141**, 15891-15900 (2019).
16. Dinh, C. T. et al. CO_2 electroreduction to ethylene via hydroxide-mediated copper catalysis at an abrupt interface. *Science* **360**, 783-787 (2018).
17. Jouny, M., Luc, W. & Jiao, F. High-rate electroreduction of carbon monoxide to multi-carbon products. *Nat. Catal.* **1**, 748-755 (2018).
18. Ripatti, D. S., Veltman, T. R. & Kanan, M. W. Carbon monoxide gas diffusion electrolysis that produces concentrated C_2 products with high single-pass conversion. *Joule* **3**, 240-256 (2019).
19. Handoko, A. D., Wei, F. X., Jenndy, Yeo, B. S. & Seh, Z. W. Understanding heterogeneous electrocatalytic carbon dioxide reduction through operando techniques. *Nat. Catal.* **1**, 922-934 (2018).
20. Hori, Y., Takahashi, R., Yoshinami, Y. & Murata, A. Electrochemical reduction of CO at a copper electrode. *J. Phys. Chem. B* **101**, 7075-7081 (1997).
21. Schouten, K. J. P., Qin, Z. S., Gallent, E. P. & Koper, M. T. M. Two pathways for the formation of ethylene in CO reduction on single-crystal copper electrodes. *J. Am. Chem. Soc.* **134**, 9864-9867 (2012).
22. Wang, L. et al. Electrochemical carbon monoxide reduction on polycrystalline copper: Effects of potential, pressure, and pH on selectivity toward multicarbon and oxygenated products. *ACS Catal.* **8**, 7445-7454 (2018).
23. Calle-Vallejo, F. & Koper, M. T. M. Theoretical considerations on the electroreduction of CO to C_2 species on Cu(100) electrodes. *Angew. Chem. Int. Ed.* **52**, 7282-7285 (2013).
24. Montoya, J. H., Shi, C., Chan, K. & Nørskov, J. K. Theoretical insights into a CO dimerization mechanism in CO_2 electroreduction. *J. Phys. Chem. Lett.* **6**, 2032-2037 (2015).
25. Luo, W. J., Nie, X. W., Janik, M. J. & Asthagiri, A. Facet dependence of CO_2 reduction paths on Cu electrodes. *ACS Catal.* **6**, 219-229 (2016).
26. Goodpaster, J. D., Bell, A. T. & Head-Gordon, M. Identification of possible pathways for C-C bond

formation during electrochemical reduction of CO_2: New theoretical insights from an improved electrochemical model. *J. Phys. Chem. Lett.* **7**, 1471-1477 (2016).
27. Xiao, H., Cheng, T. & Goddard, W. A. Atomistic mechanisms underlying selectivities in C_1 and C_2 products from electrochemical reduction of CO on Cu(111). *J. Am. Chem. Soc.* **139**, 130-136 (2017).
28. Cheng, T., Xiao, H. & Goddard, W. A. Full atomistic reaction mechanism with kinetics for CO reduction on Cu(100) from ab initio molecular dynamics free-energy calculations at 298 K. *Proc. Natl. Acad. Sci. U. S. A.* **114**, 1795-1800 (2017).
29. Garza, A. J., Bell, A. T. & Head-Gordon, M. Mechanism of CO_2 reduction at copper surfaces: Pathways to C_2 products. *ACS Catal.* **8**, 1490-1499 (2018).
30. Bagger, A., Arnarson, L., Hansen, M. H., Spohr, E. & Rossmeisl, J. Electrochemical CO reduction: A property of the electrochemical interface. *J. Am. Chem. Soc.* **141**, 1506-1514 (2019).
31. Tran, K. & Ulissi, Z. W. Active learning across intermetallics to guide discovery of electrocatalysts for CO_2 reduction and H_2 evolution. *Nat. Catal.* **1**, 696-703 (2018).
32. Kim, Y. G. et al. Surface reconstruction of pure-Cu single-crystal electrodes under CO-reduction potentials in alkaline solutions: A study by seriatim ECSTM-DEMS. *J. Electroanal. Chem.* **780**, 290-295 (2016).
33. Tang, M., Peng, H., Lamoureux, P. S., Bajdich, M. & Abild-Pedersen, F. From electricity to fuels: Descriptors for C_1 selectivity in electrochemical CO_2 reduction. *ACS Catal.* **submitted** (2019).
34. Liu, X. Y. et al. pH effects on the electrochemical reduction of $CO_{(2)}$ towards C_2 products on stepped copper. *Nat. Commun.* **10**, 32 (2019).
35. Kuhl, K. P., Cave, E. R., Abram, D. N. & Jaramillo, T. F. New insights into the electrochemical reduction of carbon dioxide on metallic copper surfaces. *Energy Environ. Sci.* **5**, 7050-7059 (2012).
36. Chan, K. & Nørskov, J. K. Electrochemical barriers made simple. *J. Phys. Chem. Lett.* **6**, 2663-2668 (2015).
37. Ng, M. L. et al. Low barrier carbon induced CO dissociation on stepped Cu. *Phys. Rev. Lett.* **114**, 246101 (2015).
38. Chan, K. & Nørskov, J. K. Potential dependence of electrochemical barriers from ab initio calculations. *J. Phys. Chem. Lett.* **7**, 1686-1690 (2016).
39. Wang, L. et al. Electrochemically converting carbon monoxide to liquid fuels by directing selectivity with electrode surface area. *Nat. Catal.* **2**, 702-708 (2019).
40. Hori, Y., Takahashi, I., Koga, O. & Hoshi, N. Electrochemical reduction of carbon dioxide at various series of copper single crystal electrodes. *J. Mol. Catal. A-Chem.* **199**, 39-47 (2003).
41. Lamoureux, P. S., Singh, A. R. & Chan, K. R. pH effects on hydrogen evolution and oxidation over Pt(111): Insights from first-principles. *ACS Catal.* **9**, 6194-6201 (2019).
42. Wang, X. et al. Mechanistic reaction pathways of enhanced ethylene yields during electroreduction of CO_2-CO co-feeds on Cu and Cu-tandem electrocatalysts. *Nat. Nanotechnol.* **14**, 1063-1070 (2019).
43. Torelli, D. A. et al. Nickel-gallium-catalyzed electrochemical reduction of CO_2 to highly reduced products at low overpotentials. *ACS Catal.* **6**, 2100-2104 (2016).
44. Weng, Z. et al. Self-cleaning catalyst electrodes for stabilized CO_2 reduction to hydrocarbons. *Angew. Chem. Int. Ed.* **56**, 13135-13139 (2017).
45. Yano, H., Shirai, F., Nakayama, M. & Ogura, K. Electrochemical reduction of CO_2 at three-phase (gas | liquid | solid) and two-phase (liquid | solid) interfaces on Ag electrodes. *J. Electroanal. Chem.* **533**, 113-118 (2002).
46. Wang, S. et al. Universal transition state scaling relations for (de)hydrogenation over transition metals. *Phys. Chem. Chem. Phys.* **13**, 20760-20765 (2011).
47. Giannozzi, P. et al. QUANTUM ESPRESSO: A modular and open-source software project for quantum simulations of materials. *J. Phys-Condens. Mat.* **21**, 395502 (2009).
48. Bahn, S. R. & Jacobsen, K. W. An object-oriented scripting interface to a legacy electronic structure code. *Computing in Science & Engineering* **4**, 56-66 (2002).
49. Wellendorff, J. et al. Density functionals for surface science: Exchange-correlation model development with bayesian error estimation. *Phys. Rev. B* **85**, 235149 (2012).
50. Monkhorst, H. J. & Pack, J. D. Special points for brillouin-zone integrations. *Phys. Rev. B* **13**, 5188-5192 (1976).
51. Henkelman, G., Uberuaga, B. P. & Jonsson, H. A climbing image nudged elastic band method for finding saddle points and minimum energy paths. *J. Chem. Phys.* **113**, 9901-9904 (2000).

52. Hammer, B. in GPAW 2013: Users and developers meeting doi: (Technical University of Denmark; 2013).
53. Trasatti, S. The absolute electrode potential: An explanatory note (recommendations 1986). *Pure Appl. Chem.* **58**, 955-966 (1986).
54. Nørskov, J. K. et al. Origin of the overpotential for oxygen reduction at a fuel-cell cathode. *J. Phys. Chem. B* **108**, 17886-17892 (2004).
55. Abild-Pedersen, F. & Andersson, M. P. CO adsorption energies on metals with correction for high coordination adsorption sites - a density functional study. *Surf. Sci.* **601**, 1747-1753 (2007).
56. Medford, A. J. et al. CatMAP: A software package for descriptor-based microkinetic mapping of catalytic trends. *Catal. Lett.* **145**, 794-807 (2015).
57. Winther, K. T. et al. Catalysis-Hub.org an open electronic structure database for surface reactions. *Scientific Data* **6**, 75 (2019).